HEALTH AND MEDICINE

A single intravenous injection of cyclosporin A–loaded lipid nanocapsules prevents retinopathy of prematurity

Marilena Bohley[1], Andrea E. Dillinger[2], Frank Schweda[3], Andreas Ohlmann[4], Barbara M. Braunger[5], Ernst R. Tamm[2], Achim Goepferich[1]*

Copyright © 2022 The Authors, some rights reserved; exclusive licensee American Association for the Advancement of Science. No claim to original U.S. Government Works. Distributed under a Creative Commons Attribution NonCommercial License 4.0 (CC BY-NC).

Retinopathy of prematurity (ROP) is a retinal disease that threatens the vision of prematurely born infants. Severe visual impairment up to complete blindness is caused by neovascularization and inflammation, progressively destroying the immature retina. ROP primarily affects newborns in middle- and low-income countries with limited access to current standard treatments such as intraocular drug injections and laser- or cryotherapy. To overcome these limitations, we developed a nanotherapeutic that effectively prevents ROP development with one simple intravenous injection. Its lipid nanocapsules transport the antiangiogenic and anti-inflammatory cyclosporin A efficiently into disease-driving retinal pigment epithelium cells. In a mouse model of ROP, a single intravenous injection of the nanotherapeutic prevented ROP and led to normal retinal development by counteracting neovascularization and inflammation. This nanotherapeutic approach has the potential to bring about a change of paradigm in ROP therapy and prevent millions of preterm born infants from developing ROP.

INTRODUCTION

More than 10% of all births worldwide are preterm, which puts millions of infants at risk for developing retinopathy of prematurity (ROP), the leading cause of childhood blindness (*1*–*3*). ROP causes vision loss and blindness via a multifactorial pathomechanism of uncontrolled retinal blood vessel growth and inflammation, which progressively destroy the retina (*3*).

Normal eye development and retinal vascularization take place in utero. In premature birth, the maternal-fetal interaction and physiologic in utero hypoxia are lost before development is complete. The newborn is now exposed to a state of hyperoxia (atmospheric oxygen as well as the frequently required use of supplemental oxygen). In addition, serum levels of insulin-like growth factor 1 (IGF1) are low at this time. Hyperoxia and low serum levels of IGF1 stop normal retinal vessel development (phase 1 of ROP). Subsequently, as the retina becomes increasingly metabolically active, it suffers from hypoxia because it is not properly vascularized (*2*, *3*). Hypoxia and the loss of maternal-fetal interaction prime retinal pigment epithelial (RPE) cells to excessively produce and secrete growth factors and cytokines such as the proangiogenic vascular endothelial growth factor (VEGF) and proinflammatory interleukins (ILs). Together, they drive the onset and progression of ROP (phase 2 of ROP) (*4*–*6*).

In high-income countries, ROP treatment consists of strictly controlling oxygen administration to avoid hyperoxia, using laser or cryotherapy to combat neovascularization or using intravitreal injections of anti-VEGF antibodies and aptamers—the current gold standard therapy (*3*, *7*). These therapies require appropriate medical infrastructure and trained personnel, which are difficult or impossible to access in most middle- and low-income countries (*8*). Because preterm birth rates are substantially higher in these countries, many infants are at risk for permanent vision loss because of ROP (*9*–*12*). Global health services recognize the severity of this problem, but there are no therapeutic approaches available that are suitable for hospitals and treatment centers in most parts of the world (*13*).

Although intravitreal anti-VEGF treatments can be used to efficiently suppress VEGF-related neovascularization, nonspecifically depriving the immature retina of VEGF comes at the price of serious adverse effects. As VEGF is a crucial growth and survival factor for various retinal cells including photoreceptors, astrocytes, ganglion, Müller, and RPE cells (*7*, *14*), the spatially uncontrolled VEGF knockdown induces cell death, tissue degeneration, retinal destruction, and detachment (*15*, *16*). The rigorous VEGF neutralization may even lead to ROP recurrence by causing hypoxia because of delayed or incomplete retinal vessel development (*17*). Intravitreally applied anti-VEGF agents have also been shown to enter the systemic circulation, reduce serum VEGF levels, and, consequently, impair the development of the brain and other organs (*18*). As anti-VEGF therapeutics are associated with such high-stake risks, we believe that all infants suffering from ROP deserve a better treatment option.

Intravenous injections are a much more accessible route of drug delivery compared to intravitreal injections, as they do not require specialized equipment or personnel. However, an intravenous therapy to efficiently treat ROP would need to target the RPE after systemic administration, which is difficult because the tissue escapes drug therapy (*19*–*21*). Simple systemic drug administration, which would build up relevant RPE drug levels, would trigger severe side effects throughout the rest of the body (*22*). To solve this problem, we have designed nanoparticles that efficiently accumulate in the RPE following intravenous injection, build a depot, and deliver the antiangiogenic, anti-inflammatory, and immune-modulating drug cyclosporin A (CsA).

To reach the RPE after systemic administration, nanoparticles need to permeate through the endothelial cell layer of the choriocapillaris and Bruch's membrane (Fig. 1) (*23*, *24*). To meet this challenge, we used lipid nanocapsules (LNCs) that mimic very-low-density lipoprotein (VLDL) particles. VLDL particles have a diameter

[1]Department of Pharmaceutical Technology, University of Regensburg, 93053 Regensburg, Germany. [2]Department of Human Anatomy and Embryology, University of Regensburg, 93053 Regensburg, Germany. [3]Department of Physiology, University of Regensburg, 93053 Regensburg, Germany. [4]Department of Ophthalmology, Munich University Hospital, Ludwig-Maximilians-University Munich, 80336 Munich, Germany. [5]Institute of Anatomy and Cell Biology, Julius-Maximilians-University of Wuerzburg, 97070 Wuerzburg, Germany.
*Corresponding author. Email: achim.goepferich@chemie.uni-regensburg.de

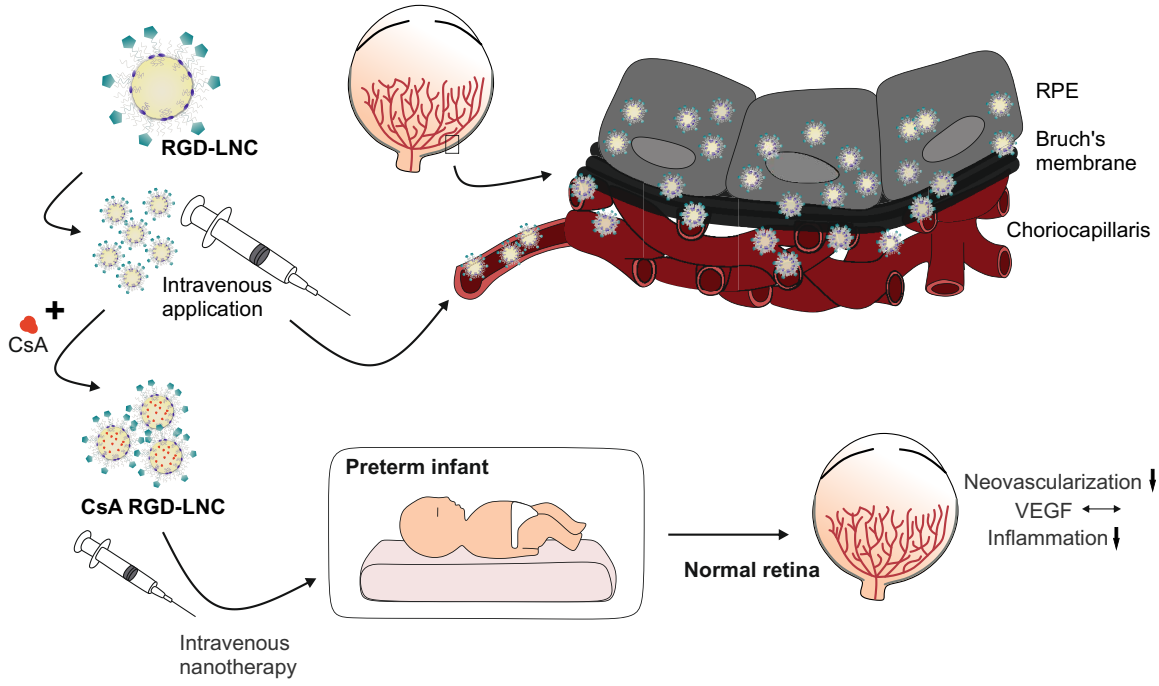

Fig. 1. Illustration of the drug delivery and therapeutic concept. Upon intravenous injection, biomimetic RGD-LNCs follow the route of VLDL. They extravasate from the choriocapillaris, diffuse through the Bruch's membrane, and accumulate in the RPE. Loaded with antiangiogenic and anti-inflammatory CsA, a simple intravenous injection of the nanotherapeutic has the potential to prevent preterm infants from developing ROP as the therapy counteracts pathologic neovascularization by normalizing VEGF expression and suppresses inflammation.

of around 60 nm and are naturally able to cross the relevant biological barriers and supply RPE cells with lipids (*25*–*28*). Our lipoprotein mimetic LNCs have a triglyceride core and a phospholipid shell that facilitates choroidal extravasation and particle uptake by binding to lipoprotein receptors such as the scavenger receptor CD36 on RPE cells (*25*, *29*). To further increase nanoparticle avidity to RPE cells and secure endothelial cell recognition to enable choroidal extravasation, LNCs were outfitted with cyclo(-Arg-Gly-Asp-D-Phe-Cys) (cRGD) tethered to the particle corona. cRGD is a ligand with nanomolar affinity for αvβ3 and αvβ5 integrins expressed by RPE and endothelial cells (*30*, *31*). When cRGD and phospholipids are present in the same particle, it is capable of heteromultivalent binding, increasing the specificity and avidity for the target cells and further enabling the nanocapsules to overcome the choroidal endothelial cell barrier (*32*).

First, we assessed the interaction of the heteromultivalent cRGD-decorated LNCs (RGD-LNCs) with endothelial and RPE cells and determined their cellular internalization in vitro. To verify the approach to target RPE cells after systemic administration, we assessed the distribution and targeting efficacy of RGD-LNCs delivered by intravenous injection in healthy mice. Then, we loaded the nanocapsules with the antiangiogenic, anti-inflammatory, and immunomodulatory CsA. CsA can suppress the VEGF signaling pathway at various intracellular sites. It counteracts the transforming growth factor–β (TGFβ)–related VEGF production in RPE cells, which is the main source of VEGF in the retina and inhibits VEGF receptor type 2 (VEGF-R2) glycosylation and trafficking. CsA also has anti-inflammatory potential and has been shown to decrease IL-1β levels in vitro (*33*–*35*). Furthermore, CsA has been demonstrated to counteract the hypoxia-induced loss of retinal ganglion cells and prevent disease-associated retinal thinning (*36*). As CsA has additionally been shown to alleviate progression of diabetic retinopathy significantly but moderately after oral administration to transplantation patients (*37*), it is a highly promising candidate to interfere with the ROP pathomechanism. We explored the therapeutic potential of CsA-loaded RGD-LNCs (CsA RGD-LNCs) in mice with oxygen-induced retinopathy (OIR), a standard mouse model for ROP. By analyzing the levels of VEGF, VEGF-R2, glial fibrillary acidic protein (GFAP), and IL-1β in both the sensory retina and RPE, we elucidated whether the nanotherapeutic truly addresses all RPE-related pathomechanisms. The overall aim was to explore whether a single intravenous injection of such a simple nanotherapeutic could prevent ROP and allow normal retinal development.

RESULTS

Lipoprotein-mimetic heteromultivalent RGD-LNCs address RPE and endothelial cells

Lipoprotein-mimetic RGD-LNCs with a diameter of 55 to 60 nm and slightly negative surface charge (Fig. 2, A to C) were prepared using a phase inversion technique to prepare the LNCs and a postinsertion technique to anchor DSPE-PEG-cRGD conjugates into the LNC shell as previously described (*38*). In a first set of experiments, we investigated the interaction of the lipoprotein-mimetic heteromultivalent RGD-LNCs with endothelial and RPE cells and determined their cellular internalization in vitro. Alongside RPE cells, we used endothelial cells to study the cellular uptake. While the former are the ultimate target, the latter are part of the barrier that the nanotherapeutic needs to overcome on its way from the

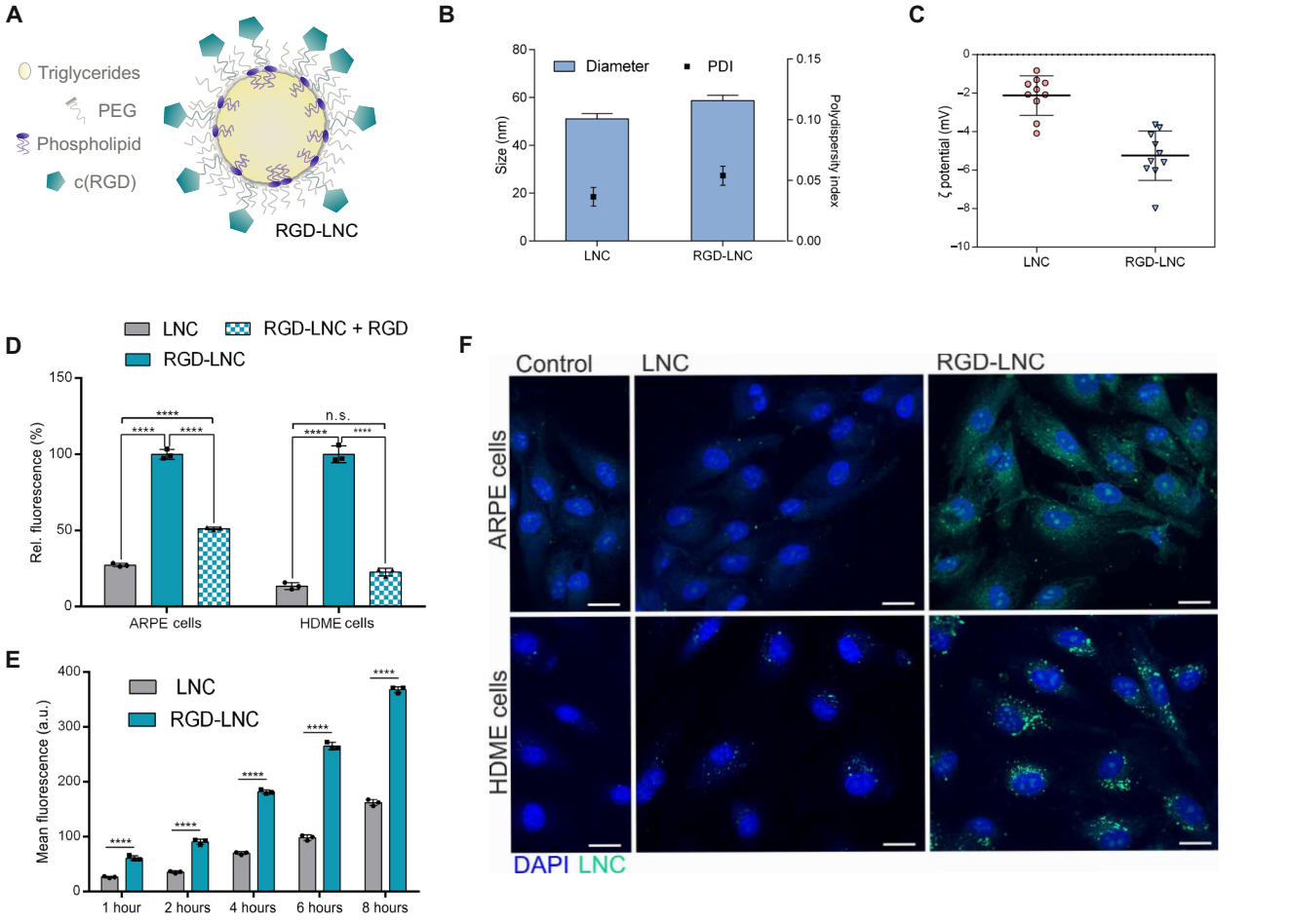

Fig. 2. VLDL-mimicking and integrin-addressing NLCs target RPE and endothelial cells. (**A**) Schematic illustration of the VLDL-mimicking nanocapsule composition and the heteromultivalent targeting concept of RGD-LNCs. (**B**) Hydrodynamic diameter and polydispersity index (PDI) of LNCs and RGD-LNCs. (**C**) ς potential of LNCs and RGD-LNCs. (**D**) Ligand-mediated cellular uptake of LNCs and RGD-LNCs in human RPE (ARPE) cells and human dermal microvascular endothelial (HDME) cells, partially inhibited by free cRGD. (**E**) Ligand-mediated uptake kinetic of LNCs and RGD-LNCs in ARPE cells. (**F**) Cellular localization of LNCs and RGD-LNCs in HDME and ARPE cells. Scale bars, 20 μm. Results are presented as means ± SD of $n = 10$ (B and C) independent experiments and $n = 3$ (D and E) biologically independent samples per group. Levels of statistical significance are indicated as $^{****}P \leq 0.0001$. n.s., nonsignificant. *P* values were determined by two-way analysis of variance (ANOVA) (D) and one-way ANOVA (E). DAPI, 4′,6-diamidino-2-phenylindole.

blood to the retina. Similar results were obtained for both cell types (Fig. 2D). While the cellular uptake of control LNCs was only moderate, RGD-LNCs were taken up excessively.

This confirmed the benefits of the heteromultivalent nanoparticle design. The two targeting moieties, cRGD and the phospholipid, were of significant advantage for RPE cell recognition and internalization. The significance of the integrin ligand was further demonstrated by the sharp decrease of cellular uptake of RGD-LNCs when αvβ3 and αvβ5 integrin receptors were blocked with free cRGD (Fig. 2D). Cellular uptake of both RGD-LNCs and LNCs into RPE cells increased continuously with time (Fig. 2E), which can be attributed to phospholipid-mediated uptake via the scavenger receptor CD36 that both particle species bind to. The internalization of the nanocapsules into cells was confirmed using fluorescence microscopy. Figure 2F shows that RGD-LNCs are exclusively located in the cytosolic region of both cell types and that there is no unspecific adhesion to the cell surface.

RGD-LNCs accumulate in the RPE after intravenous injection

To investigate the in vivo fate of RGD-LNCs following intravenous injection and the efficacy of the targeting strategy, we first assessed their whole-body distribution relative to their ocular accumulation in healthy mice. The amount of accumulated nanocapsules determined by fluorescence spectroscopy served as a proxy for biodistribution. One hour after injection, approximately 10% of the administered dose [initial dose (ID)] of RGD-LNCs reached the posterior eye per gram of tissue (Fig. 3A), which is equivalent to 2.0% of the total administered dose of RGD-LNCs accumulating in the retina (Fig. 3B). Given the low mass and the challenge of accessing the retina, this is an outstanding targeting efficacy compared to other nanotherapeutics (*39*, *40*). In addition, the results rigorously support the advantage of the heteromultivalent nanocapsule design because ocular enrichment is eight times higher for RGD-LNCs compared to LNCs (Fig. 3A). After proving that targeted RGD-LNCs accumulate in the eye after intravenous injection, the next step was to elucidate the

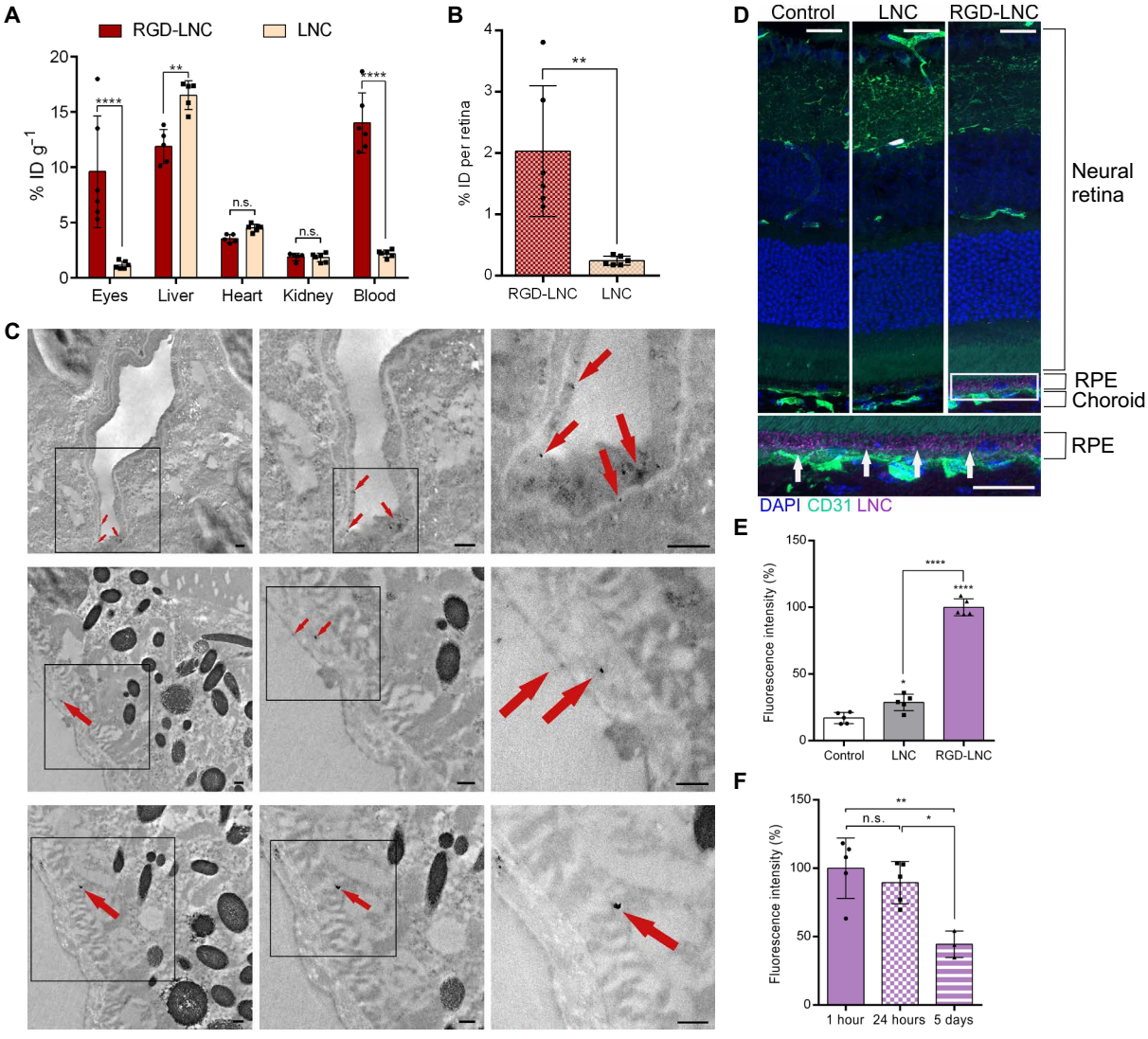

Fig. 3. Effective and RPE-specific intraocular RGD-LNC enrichment. (**A**) Nanocapsule accumulation after intravenous administration and 1 hour of blood circulation in % ID per gram of tissue in healthy mice. (**B**) Absolute target tissue distribution in % ID of RGD-LNCs and LNCs in the retina. (**C**) TEM images showing dual RGD-LNCs in the posterior eye 1 hour after intravenous administration. Top: RGD-LNCs are associated with endothelial cells. Middle: RGD-LNCs adjacent to and migrating in the Bruch's membrane. Bottom: RGD-LNCs internalized in RPE cells. Arrows indicate electron-dense superparamagnetic iron oxide nanoparticles (SPIONs) containing dual RGD-LNCs. From left to right: Squared out regions show progressive magnification. Scale bars, 250 nm. Representative images of at least $n = 5$ biologically independent samples. (**D**) Sagittal section of eyes stained for endothelial cells (CD31; green) and cell nuclei (DAPI; blue) showing RPE-specific accumulation of RGD-LNCs 1 hour after intravenous administration. Nanocapsule accumulation in the RPE is indicated with white arrows. Lilac: Nanocapsule-associated fluorescence. Squared out region shows magnification. Scale bars, 20 μm. (**E** and **F**) Quantitative analysis of nanoparticle fluorescence 1 hour after administration of LNCs or RGD-LNCs (E) and of RGD-LNCs at different time points (F). Results are presented as means ± SD of $n = 6$ (A and B) mice per treatment group, $n = 5$ (E), or at least $n = 3$ (F). Levels of statistical significance are indicated as $^{*}P \leq 0.05$, $^{**}P \leq 0.01$, and $^{****}P \leq 0.0001$. *P* values were determined by two-way ANOVA (A), unpaired *t* test (B), and one-way ANOVA (E and F).

targeting mechanism. We were curious whether the lipoprotein mimetic lipid nanoparticles truly follow the route of VLDL, extravasate from choroidal vessels, and ultimately reach and accumulate in the RPE. Previous in vivo experiments demonstrated that cRGD-grafted quantum dots bind to choroidal endothelial cells but are not able to extravasate from the bloodstream and reach RPE cells (*41*). Thus, we were keen to investigate whether the lipoprotein-mimetic approach would overcome this limitation.

To visualize LNCs using both fluorescence microscopy and transmission electron microscopy (TEM), LNCs that are simultaneously loaded with fluorescent dye and electron dense superparamagnetic iron oxide nanoparticles (SPIONs) (=dual LNCs) were used (fig. S1, A and B) (*42*). TEM imaging allowed us to assess the exact cellular localization of dual RGD-LNCs in the retina of healthy mice. Figure 3C shows the presence of dual RGD-LNCs in choroidal endothelial cells, the Bruch's membrane, and RPE cells, suggesting that RGD-LNCs do follow the VLDL route toward the RPE. These findings were further supported by the fact that fluorescence microscope images taken 1 hour after intravenous injection showed excessive amounts of RGD-LNCs in the RPE (Fig. 3D). Quantifying the nanocapsules in the RPE using fluorescence density measurements revealed that both LNCs and RGD-LNCs reached the RPE

but only the heteromultivalent RGD-LNCs accumulated sufficiently in the target tissue (Fig. 3E). The heteromultivalent and lipoprotein mimetic approach successfully facilitates both choroidal vessel extravasation and target cell accumulation in vivo. Using fluorescence imaging, neither RGD-LNCs nor LNCs were found in other retinal cell types, indicating endothelial and RPE cell specificity (Fig. 3D).

In a final set of experiments regarding target efficacy, the residence time of RGD-LNCs in the RPE was evaluated by taking fluorescence images of the posterior eye 1 hour, 24 hours, and 5 days after intravenous administration. While fluorescence microscopy revealed the presence of RGD-LNCs in the RPE for all three time points, quantitative evaluation showed that the maximum accumulation was reached 1 hour after administration and remained at a constant level for at least 24 hours (Fig. 3F). Unexpectedly, after 5 days, substantial amounts of RGD-LNCs could still be detected in the target tissue, suggesting the formation of a nanocapsule depot, which is highly promising for the prospective drug therapy.

One injection of CsA RGD-LNCs inhibits neovascularization

After designing a nanocarrier that successfully accumulates in RPE cells, we assessed the therapeutic potential of CsA RGD-LNCs (fig. S1, B to D) by testing them in a mouse model of ROP. To that end, we chose the mouse model of OIR because it is considered the standard rodent model for ROP (*43*). To induce the disease, we subjected newborn mice to oxygen treatment beginning on postnatal day 7 (P7), which causes an initial loss of retinal vessels because of the hyperoxia-related suppression of VEGF levels (phase 1 of ROP). Subsequent termination of oxygen treatment on P12 leads to massive VEGF overexpression accompanied by inflammation spurring neovascularization and ROP progression (phase 2 of ROP) (*44*, *45*). On the basis of this mechanism (Fig. 4A), we treated the mice on P12 with a single intravenous injection, right before the onset of pathologic neovascularization (=phase 2 treatment). To assess the therapeutic potential of CsA RGD-LNCs, we compared the effects of CsA RGD-LNCs to the effects of equivalent doses of intravenously applied CsA solution (Sandimmun, referred to as free CsA) and phosphate-buffered saline (PBS) (referred to as control). The CsA RGD-LNC dose and free CsA concentration were chosen on the basis of the clinical standard for systemic CsA administration (*46*).

While phase 1 treatments aim to counteract hypoxia-induced changes and decrease avascularity, the most relevant metric for the therapeutic success of a phase 2 treatment aiming to fight destructive

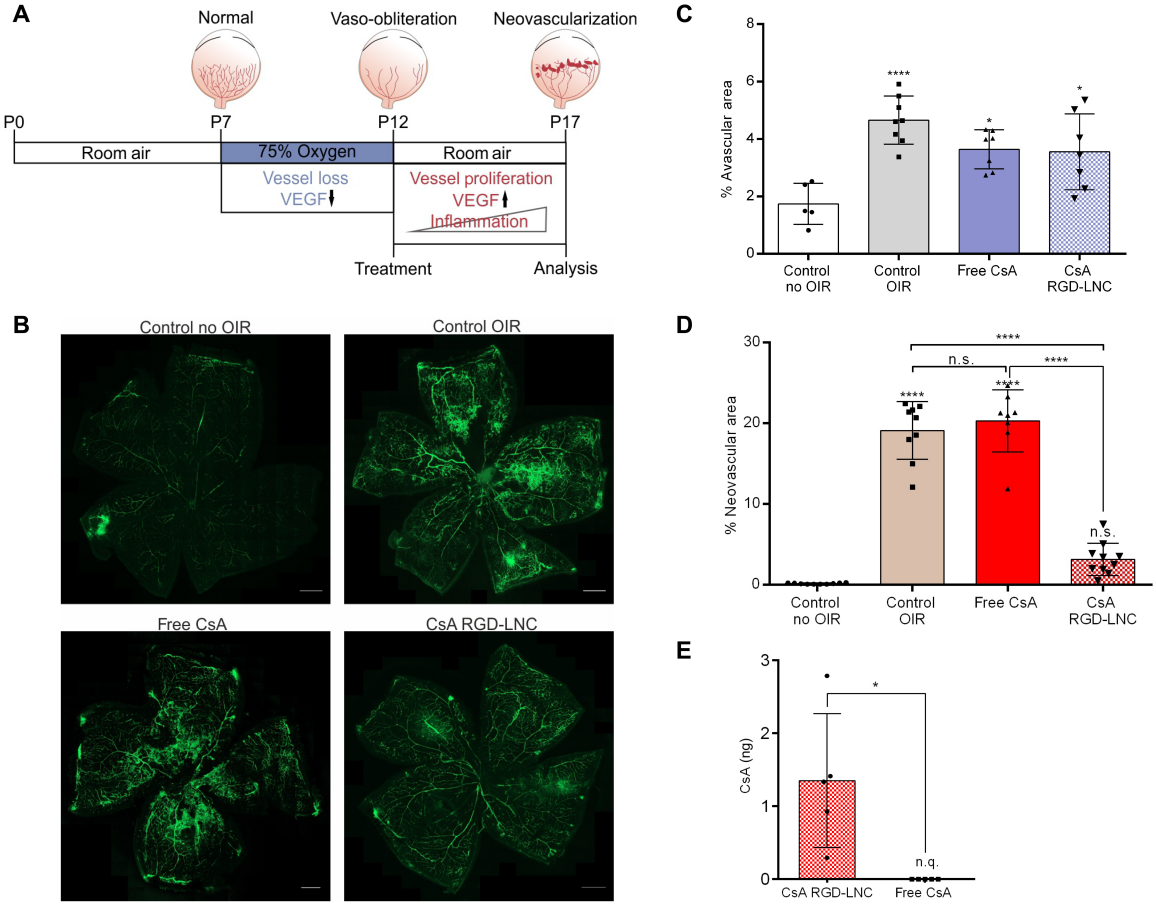

Fig. 4. CsA RGD-LNC effects on the progression and prevention of neovascularization. (**A**) Scheme depicting the pathogenesis and intervention regime in the mouse model of OIR. (**B**) Representative images of retina whole mounts showing the retinal vasculature stained with fluorescein isothiocyanate (FITC)–dextran (green) at P17. Untreated control (without OIR and with OIR; control no OIR and control OIR) compared to free CsA and CsA RGD-LNCs–treated mice. Scale bars, 500 μm. (**C**) Quantification of the relative avascular area. (**D**) Quantification of the relative neovascular area. (**E**) Absolute CsA content in the posterior eye of mice with OIR at P17 after injection of CsA RGD-LNCs or free CsA at P12. n.q., not quantifiable. Results are presented as means ± SD of at least $n = 5$ (C), $n = 8$ (D), and $n = 5$ (E) mice per treatment group. Levels of statistical significance are indicated as $^*P \leq 0.05$ and $^{****}P \leq 0.0001$. *P* values were determined by one-way ANOVA (C) and unpaired *t* test (D).

neovascularization is the degree of inhibiting retinal neovascularization (*47*). OIR treatment causes pathological changes in the retinal vasculature, as seen in Fig. 4B, which has an avascular zone in the central retina, large areas of newly formed, leaky vessels and neovascular tufts (control OIR). In contrast, the retinas of mice treated with CsA RGD-LNCs show a marked decrease of neovascular zones, leaky vessels, and neovascular tufts (Fig. 4B, CsA RGD-LNC). As expected, the treatment applied after oxygen administration and at phase 2 of ROP pathogenesis caused no effects on the avascular zone (Fig. 4C). To quantify the efficacy against neovascularization, the areas of tufts and proliferating vessels were measured, normalized to the overall retinal area, and expressed as extent of neovascularization (Fig. 4D). CsA RGD-LNCs suppressed neovascularization by a factor of 6, which reduced the levels to those of healthy control animals. An identical dose of CsA injected as aqueous solution had no effects. Impressively, just a single injection of CsA RGD-LNCs given directly after the cessation of oxygen administration delivers enough CsA to the RPE to entirely prevent ROP from developing.

On P17, drug content in the eye was analyzed using ultrahigh-performance liquid chromatography in combination with mass spectrometry (UHPLC-MS) (Fig. 4E). Even 5 days after injection, CsA was still detectable in the posterior eye of mice that received the nanocapsule formulation but not in animals treated with the free drug solution. This confirms the efficacy and necessity of the drug delivery system. Overall, the results demonstrate that RGD-LNCs are a highly precious tool for forming a depot that maintains drug concentration in the RPE for several days. This targeting strategy enables one injection of CsA RGD-LNCs to completely prevent pathologic neovascularization in a mouse model of ROP.

CsA RGD-LNCs fight the underlying RPE-related pathomechanism

Because the CsA RGD-LNCs had tremendous inhibitory effects on neovascularization, we were intrigued by the underlying mechanism. CsA prevents angiogenesis by suppressing VEGF-R2 glycosylation and intracellular trafficking. It further interferes with the VEGF signaling pathway at various intracellular sites and counteracts TGFβ-related VEGF production in RPE cells (*33*, *48*, *49*). To elucidate the mechanism of the nanotherapeutic, we quantified changes in retinal VEGF-R2 and VEGF protein levels in both the RPE-choroid complex and the neural retina of treated versus untreated mice. Immunohistochemical analysis revealed that the treatment with CsA RGD-LNCs decreased elevated VEGF-R2 levels in OIR mice down to the physiological values measured in healthy control animals (Fig. 5, A and B). For VEGF, similar results were observed, with a reduction to physiological values in both the RPE-choroid complex (Fig. 5C) and the neural retina (Fig. 5D) upon CsA RGD-LNC treatment. CsA RGD-LNCs counteract pathologic VEGF production in RPE cells and consequently reduce available amounts of VEGF in the whole retina. Overall, the results demonstrate that the nanotherapeutic counteracts VEGF-driven neovascularization by normalizing VEGF and VEGF-R2 levels.

We next explored the effects of CsA RGD-LNC therapy on inflammation (*50*). To that end, we first investigated the expression of GFAP, a marker for the reactivity of Müller cell glia. Müller cell glia react in response to retinal damages and inflammation caused by ROP in a process called gliosis. Pronounced expression of GFAP is a surrogate for retinal damage and inflammation (*51*). Figure 5F shows that in control eyes, GFAP expression was restricted to

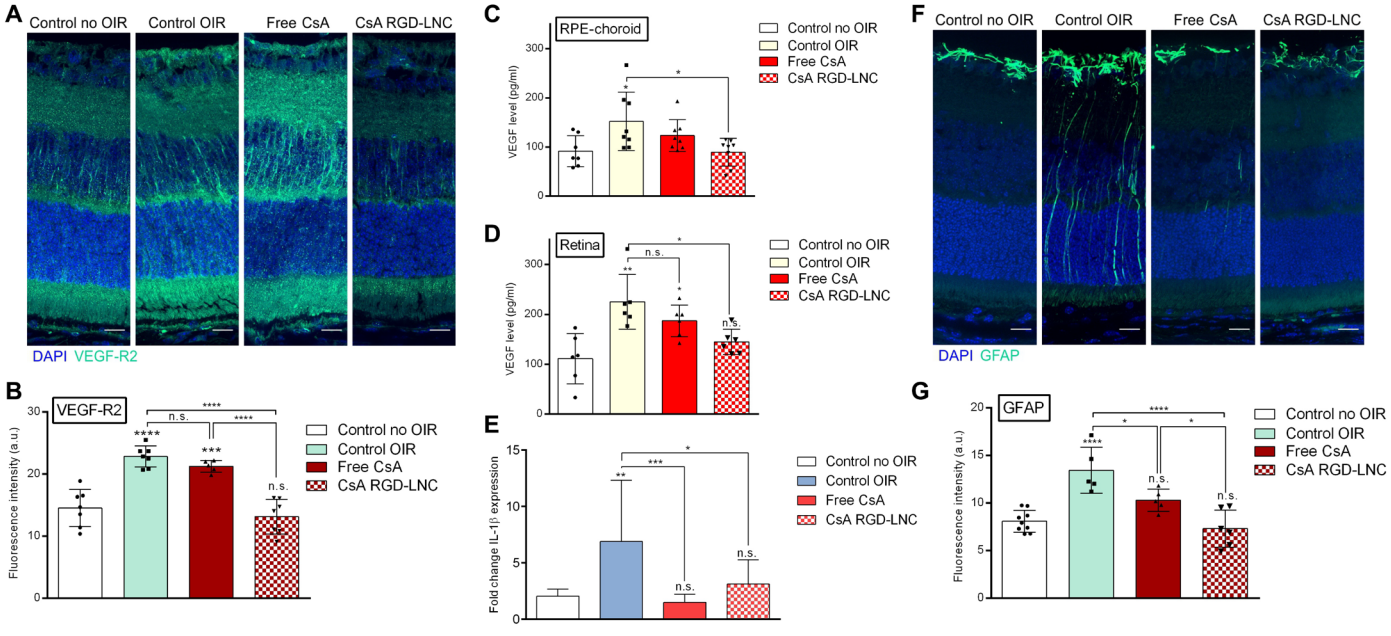

Fig. 5. Molecular angiogenic and inflammatory responses to CsA RGD-LNC therapy. (**A**) Imaging of VEGF-R2 expression in the posterior eye. Blue, DAPI staining of cell nuclei; green, VEGF-R2. (**B**) Quantitative analysis of VEGF-R2 fluorescence density from cryosections immunohistochemically stained with VEGF-R2 antibody (A). (**C** and **D**) Assessment of VEGF protein levels in (C) the RPE-choroid complex and (D) the neural retina determined through ELISA. (**E**) Quantification of IL-1β mRNA expression levels in RPE-choroid complex using reverse transcription quantitative polymerase chain reaction (RT-qPCR). (**F**) Imaging of GFAP expression in the posterior eye. Blue, DAPI staining of cell nuclei; green, GFAP. (**G**) Quantitative analysis of GFAP fluorescence from sections shown in (F). Scale bars, 20 μm. Results are presented as means ± SD of at least $n = 5$ (A, B, and E to G) and $n = 6$ (C and D) mice per treatment group. Levels of statistical significance are indicated as $^{*}P \leq 0.05$, $^{**}P \leq 0.01$, $^{***}P \leq 0.001$, and $^{****}P \leq 0.0001$. *P* values were determined by one-way ANOVA (A to F).

Müller cell end feet, which are located at the inner retinal surface. In OIR eyes, GFAP expression was seen throughout the whole retina, indicating Müller cell reactivity and typical gliosis reaction due to inflammation and retinal damages caused by OIR. The treatment with the nanotherapeutic led to a significant decrease of the inflammatory marker down to normal values (Fig. 5G). Together with the significantly lower production of proinflammatory IL-1β mRNA in RPE cells (Fig. 5E), these data highlight the anti-inflammatory effects of CsA RGD-LNCs.

Together, the mechanistic investigation revealed bright prospects for the comprehensive treatment of ROP, as CsA RGD-LNCs normalize vascularization by restoring natural VEGF and VEGF-R2 levels and substantially reduce inflammation.

CsA RGD-LNCs as a therapy for all infants at risk of ROP

So far, the investigations revealed that a single dose of CsA RGD-LNCs halts the pathogenesis of ROP by restoring vital growth factor and cytokine levels. This success prompted us to evaluate the potential of CsA RGD-LNCs as a preemptive treatment for preterm infants at risk of developing ROP. A successful preventive therapy must prevent the condition but also have no negative effects on healthy eyes that are not developing ROP. To that end, we treated healthy mice with CsA RGD-LNCs (Fig. 6A). Investigation of the vessel status revealed no alteration and no disturbance of normal vessel development after treatment (Fig. 6, B and C, and fig. S2, A and B). The prophylactic intervention caused no significant changes in the VEGF and VEGF-R2 expression of healthy animals (Fig. 6, D, F, and H, and fig. S2, C to F). This reassured us that VEGF signaling, which is essential for physiological vessel development and overall ocular homeostasis and integrity, remained unaffected in mice without OIR that were treated with CsA RGD-LNCs. GFAP protein and IL-1β mRNA levels were also unaffected (Fig. 6, E, G, and I, and fig. S2G). The use of CsA RGD-LNCs caused no morphological changes in the retinas of mice with or without OIR (fig. S3), supporting their safe use.

DISCUSSION

The overarching goal of this work was to develop a treatment for ROP that counteracts the underlying pathomechanism of neovascularization and inflammation while avoiding complex and expensive medical techniques unavailable to patient populations in middle- and low-income countries. To meet this challenge, we designed a simple nanotherapeutic that prevents ROP development by a single intravenous injection.

Our formulation takes inspiration from nature, using LNCs that mimic VLDL and adding targeting ligands (cRGD) so they can cross the necessary biological barriers and accumulate in the target

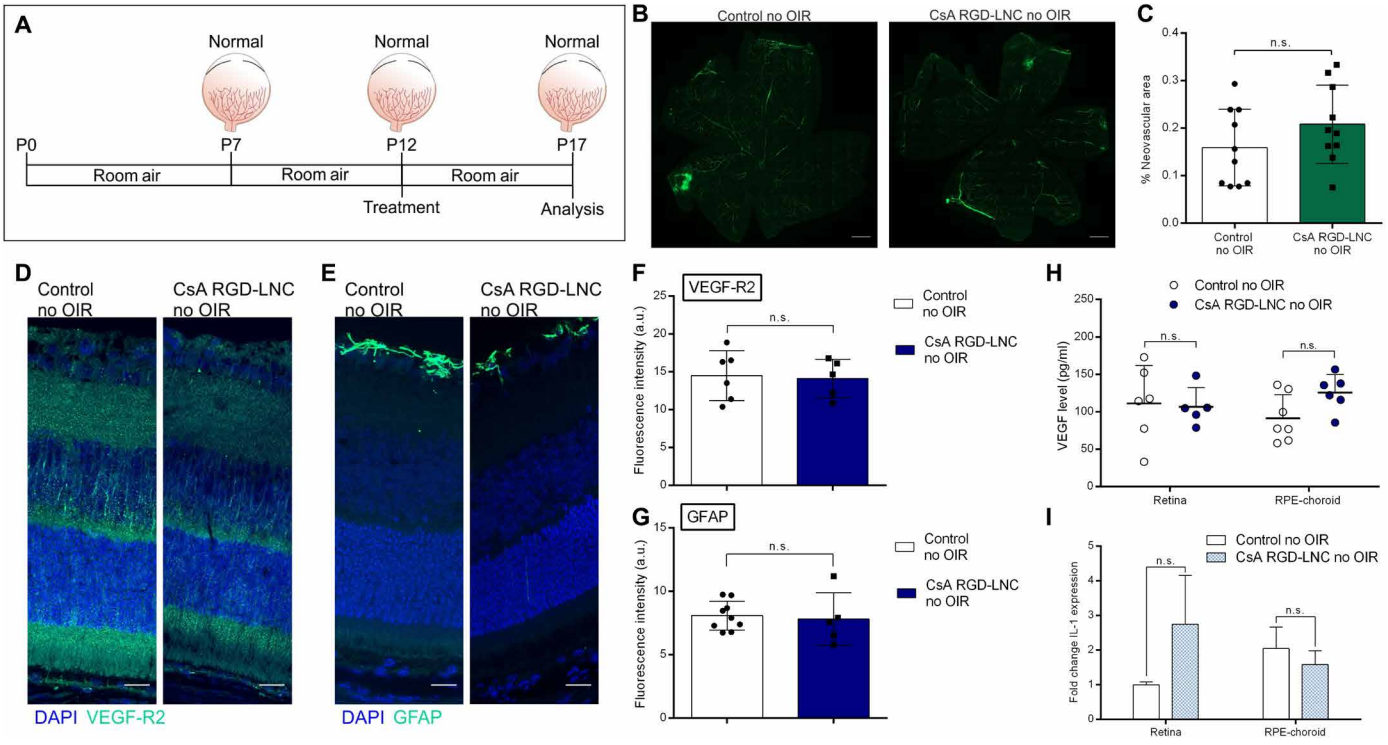

Fig. 6. Clinical and molecular ocular effects of CsA RGD-LNC therapy on healthy mice. (**A**) Scheme depicting the intervention regime for mice without OIR. (**B**) Representative images of retina whole mounts showing the retinal vasculature. Green, FITC-dextran. Scale bars, 500 μm. (**C**) Quantification of the relative neovascular area. (**D**) Imaging of VEGF-R2 expression in the eye. Blue, DAPI staining of cell nuclei; green, VEGF-R2. (**E**) Imaging of GFAP expression in the eye. Blue, DAPI staining of cell nuclei; green, GFAP. (**F**) Quantitative analysis of VEGF-R2 fluorescence from sections shown in (D). (**G**) Quantitative analysis of GFAP fluorescence from sections shown in (E). (**H**) Assessment of VEGF protein levels in the neural retina and RPE-choroid complex through ELISA. (**I**) Representation of IL-1β mRNA level fold change in the neural retina and RPE-choroid complex determined through RT-qPCR. Scale bars, 20 μm. Results are presented as means ± SD of at least $n = 5$ (F, G and I), $n = 6$ (H), and $n = 10$ (C) mice per treatment group. *P* values were determined by unpaired *t* test (C, F, and G), multiple *t* test (I), and two-way ANOVA (H).

tissue. RGD-LNCs successfully mimicked VLDL particles and were able to enrich in RPE cells following intravenous injection. As expected, they were not exclusively distributed to the posterior eye but, like other nanoparticles, in the whole organism (*52*). However, our findings show how remarkable these particles are in their ability to target the RPE: Only LNCs that carried cRGD accumulated efficiently in the RPE, proving that the heteromultivalent targeting of avβ3 and avβ5 integrins is essential. Their ability to recognize target cells was highly efficient because RGD-LNCs accumulated massively in the RPE when compared to liver tissue, which is a part of the mononuclear phagocytic system and able to actively remove particles from the central circulation (*24*). Within the eye itself, particles were found exclusively in endothelial and RPE cells, suggesting that this design achieves retinal cell-specific drug delivery. Although there are other drug delivery systems available using active targeting to specifically address RPE cells upon intravenous injection, none revealed target cell specificity (*20*, *53*, *54*).

Compared to control LNCs, RGD-LNCs had prolonged residence time and higher concentrations in the blood. This suggests that particles persist in circulation for over 1 hour, giving them more time to reach the target tissue and making it likely that lower doses could be used in future experiments. In addition, RGD-LNCs had a remarkable residence time in the RPE, with a significant quantity of nanocapsules present even 5 days after injection. This depot formation in the RPE is highly advantageous for the delivery of drugs, as sustained drug release would counterbalance rapid ocular drug clearance (*22*). With the RPE playing a pivotal role in the onset and progression of various retinal diseases, this drug delivery system provides a valuable tool for the development of novel approaches to treat diseases with RPE-associated pathomechanisms such as diabetic retinopathy and age-related macular degeneration (*4*).

After confirming that our nanoparticle system effectively targets the cell population involved in the mechanism underlying ROP, we chose CsA as drug candidate because it addresses all relevant arms of disease development. We found that CsA RGD-LNCs were remarkably successful in vivo. A single intravenous dose of CsA RGD-LNCs completely prevented neovascularization and ROP development. While intravitreal anti-VEGF agents have been shown to increase avascularity and resulting hypoxic injuries in the retina during phase 1 of ROP progression, CsA RGD-LNCs did not affect the avascular zone (*55*). We confirmed that the observed effects on neovascularization occurred because CsA RGD-LNCs effectively down-regulated VEGF and VEGF-R2 levels. In contrast to the contemporary clinical practice of anti-VEGF therapy that reduces VEGF levels to zero (*56*), our nanotherapeutic reduced VEGF and VEGF-R2 expression to healthy levels. This is highly advantageous because physiological VEGF levels are vital for normal retinal development and for the survival of various retinal cells including photoreceptors, astrocytes, ganglion, Müller, and RPE cells (*15*). This measured approach to regulating VEGF levels will minimize the risk of negative effects and reduce the need for additional treatments. Besides showing the valuable therapeutic effect of "normalizing" vessel growth, our results shed light on the anti-inflammatory potential of CsA RGD-LNCs. Retinal GFAP levels that correlate with the degree of retinal damage and inflammatory processes were found to be significantly lowered after treatment with the nanotherapeutic. The anti-inflammatory effect of our nanotherapeutic was further supported by the significant decrease of proinflammatory IL-1β mRNA expression. While the antiangiogenic and anti-inflammatory effects of CsA were leveraged to combat ROP development and progression, the immune-modulatory potential of CsA can be helpful when an infant concomitantly suffers from ROP and fetal inflammatory response syndrome (FIRS). Current studies suggest a correlation between FIRS and ROP, indicating that FIRS predisposes to ROP (*57*). FIRS is driven by excessive systemic T lymphocyte activation and IL release. As CsA can counteract both, we hypothesize that treating infants suffering from FIRS and ROP with the nanotherapeutic could have synergistic effects on both diseases.

While our intravenous approach, such as intravitreal anti-VEGF injections, represents a phase 2 treatment for ROP, there are other systemic approaches aiming to interfere at phase 1of ROP development. During the initial period of hyperoxia, a large avascular zone in the central retina develops. It is this area that becomes hypoxic due to insufficient blood perfusion. Consequently, hypoxia-induced or hypoxia-regulated factors are up-regulated, which trigger production and secretion of growth factors from the RPE and, thus, neovascularization (*7*). It has been shown that stabilizing hypoxia-inducible factors, which are transcription factors that modulate adaptation to hypoxia, can prevent neovascularization (*58*–*60*). One limitation that all phase 1 approaches share is that they must be applied in a brief window of opportunity to successfully interfere with these mechanisms to prevent retinal neovascularization. If administered too late, they exhibit adverse effects and even promote destructive neovascularization (*59*). In addition, although they are applied at the exact time point, they are ineffective against inflammation that contributes significantly to both onset and progression of ROP. The same holds true for oral administration of propranolol, another phase 1 approach. Although it has been shown to prevent astrocyte degeneration resulting from hypoxic injuries, it failed to completely prevent ROP and is ineffective against inflammation (*61*). Another phase 1 treatment approach is intravenous injections of recombinant human IGF1 complexed with its binding protein (rhIGF1/rhIGFBP3). This therapy did not reveal any effects on ROP severity or ROP occurrence in a phase 2 trail (*62*). Together, although some phase 1 treatment approaches pose therapeutic potential for preventing avascularity and, thus, inhibiting destructive neovascularization, they must be administered at the exact time point regarding ROP pathogenesis and do not affect other underlying pathomechanisms. Both limitations render these approaches impractical or even ineffective in a clinical setting, especially under the basic medical conditions in middle- and low-income countries.

Challenging healthy mice with the nanotherapeutic did not elicit any negative effects on the development of the retinal vasculature or overall retinal morphology. This suggests that CsA RGD-LNCs could be used as a preemptive treatment (independent of ROP disease stage), which is applied directly after the oxygen treatment, without the need of complex and costly diagnostics that are unavailable in most parts of the world. The development of a preventive treatment for ROP with the simplicity of intravenous injection and the need for only a single application would be of paramount value particularly for middle- and low-income countries, where the prevalence of ROP is high and the diagnostic and therapeutic possibilities are low (*9*, *10*). While further research regarding toxicity, dosing, and long-term effects is needed, the biggest hurdle to translate the nanotherapeutic into clinics is the lack of commercial interest. In industrial countries, the prevalence of ROP is rather low and there

are different therapies available; consequently, there is no financial interest in developing a new ROP treatment. Once this hurdle has been overcome, this work provides the basis for a single-dose intravenous treatment as standard therapy for all infants at risk for ROP.

MATERIALS AND METHODS

Materials

Kolliphor HS15 was obtained from BASF, and Lipoid S75-3 was acquired from Lipoid GmbH (Ludwigshafen, Germany). Miglyol 812 [medium chain triglycerides (MCT)] was purchased from Caesar & Loretz GmbH (Hilden, Germany). 1,1′-Dioctadecyl-3,3,3′,3′-tetramethylindocarbocyanine perchlorate (DiI) was purchased from Invitrogen (Waltham, USA). Sodium oleate was purchased from TCI Europe (Zwijindrecht, Belgium). CsA was obtained from Pharma Stulln GmbH (Stulln, Germany). 1,2-Distearoyl-*sn*-glycero-3-phosphoethanolamine-*N*[maleimide(polyethyleneglycol)-2000] (ammonium salt) (DSPE-PEG2000-maleimide) was purchased from Avanti Polar Lipids Inc. (Alabaster, USA). cRGD acetate salt was purchased from Bachem Distribution Service GmbH (Weil a. Rhein, Germany). Dulbecco's PBS (DPBS) was acquired from Gibco Life Technologies (Waltham, USA). Purified water was obtained from a MilliQ System from Millipore (Schwalbach, Germany). All other materials and reagents in analytical grade were obtained from Merck (Taufkirchen, Germany).

Lipid nanoparticle preparation and characterization

LNCs were prepared after Heurtault et al. (*63*), with slight modifications as previously described (*38*). In short, 887.5 mg of Kolliphor HS15 40% (w/w), 30 mg of Lipoid S75-3, 415 mg of MCT, 12 mg of NaCl, and 655.8 mg of water were heated in a phase inversion process of three cycles between 90° and 60°C. In the third cycle, water was added at the phase inversion temperature, leading to stable LNC formation. The final dispersion was filtered through a 0.22-μm regenerated cellulose membrane for sterilization and stored at room temperature (RT) in the dark. For particle detection, fluorescent dyes [1.5% DiI (w/w)] and/or SPION 0.24% iron (w/w) were added to the initial mixture (*42*). For the preparation of CsA-loaded LNCs (34 mg of CsA/g LNC), MCT was replaced by 8.5% (w/w) CsA-MCT solution, and particles were prepared as described above. For cRGD peptide grafting, cRGD was first coupled to DSPE-PEG2000-maleimide (2 hours, RT, 500 rpm). Next, the conjugates were inserted in the shell of the LNC by using the postinsertion method as previously described (3 hours, 37°C, 500 rpm) (*64*). For purification and concentration, both unmodified LNCs and modified LNCs were dialyzed against DPBS overnight using Spectra/Por Float-A-Lyzer G2 300-kDa molecular weight cutoff (MWCO) and subsequently washed twice with 4 ml of DPBS (15 min, RT, 4000*g*) using a 100-kDa MWCO Amicon Ultra-4 centrifugal device. Size and ξ potential of the resulting particles were measured in 10% DPBS (v/v) at a constant temperature of 25°C using 2 mg/ml concentrations with a ZetaSizer Nano ZS (Malvern Instruments). To assess the CsA content and the encapsulation efficacy, CsA LNCs were diluted with methanol and ultrasonicated (30 min) to disrupt the particles. Afterward, CsA was quantified by UHPLC-MS, as previously described (*38*).

Cell culture

Human dermal microvascular endothelial (HDME) cells were cultured in endothelial cell growth medium MV (GM) and endothelial cell basal medium MV (BM), all purchased from PromoCell GmbH (Heidelberg, Germany; catalog no. C-12210). HDME cells were used in low passage numbers ranging from 4 to 7. Human retina pigment epithelial cells (ARPE-19 a spontaneously arising retinal pigment epithelia cell line derived from the normal eye; RRID: CVCL_0145), gifted by U. Friedrich (Institute of Human Genetics, University of Regensburg), were cultured in Dulbecco's modified Eagle's medium (DMEM)–F12 (1:1) supplemented with 10% fetal bovine serum obtained from Biowest (Nuaillé, France).

Cellular targeting

Particle uptake through flow cytometry was performed as previously described (*38*). In short, either HDME or ARPE-19 cells were seeded in 24-well plates at a density of 50,000 cells per well and incubated in BM or DMEM-F12 (1:1) for 24 hours (37°C). Prewarmed particle solutions [0.6 mg/ml in Leibovitz medium supplemented with 0.1% bovine serum albumin (BSA)] were added to the cells, after washing them with DPBS, and incubated for 1 hour. To confirm the ligand specificity, cells were incubated with cRGD solution (1 mg/ml) before particle addition. Afterward, particle solutions were discarded, and the cells were washed twice with DPBS, trypsinated, and centrifuged (200*g*, 5 min, 4°C). Nanoparticle-associated cell fluorescence was analyzed in DPBS using a FACSCanto II cytometer (Becton Dickinson). The population of viable cells was gated using Flowing software 2.5.1. (Turku Centre for Biotechnology), and the geometric mean of the nanoparticle associated fluorescence was analyzed.

For the assessment of particle uptake kinetics, ARPE-19 cells were seeded in 24-well plates at a density of 50,000 cells per well and incubated in DMEM-F12 (1:1) for 24 hours (37°C). After washing the cells with DPBS, prewarmed particle solutions (0.6 mg/ml in Leibovitz medium supplemented with 0.1% BSA) were added to the cells and incubated for 1, 2, 4, 6, and 8 hours. After all incubation periods, cells were processed and analyzed as described above. To determine the cellular distribution of the different particle formulations, HDME and ARPE-19 cells were seeded in coverslip containing six-well plates at a density of 300,000 cells per well and incubated over 24 hours. Then, cells were washed with DPBS and incubated with prewarmed particle solutions (0.6 mg/ml in Leibovitz medium supplemented with 0.1% BSA) for 1 hour. Afterward, the solutions were discarded, and before the fixation with 4% paraformaldehyde (PFA), cells were washed thoroughly with DPBS. The coverslips were then transferred onto Superfrost plus glass slides, and cell nuclei were stained with 4′,6-diamidino-2-phenylindole (DAPI) (0.15 μg/ml) before imaging using an Axio Imager fluorescence microscope with a Plan-Neofluar 40×/1.30 oil M27 objective (Carl Zeiss AG) and the Zen software (Carl Zeiss Microscopy).

In vivo distribution and targeting

The in vivo distribution experiments were carried out according to the national and Institutional Animal Care and Use Committee (IACUC) guidelines and were approved by the local authority (Regierung von Unterfranken, reference number: 55.2-2532-2-329). As animal models, 10-week-old female 129SV mice (Charles River Laboratories, Sulzfeld, Germany; strain code: 287) were used. The different nanoparticle solutions [LNC or RGD-LNC (10 mg/ml) in DPBS] were injected (100 μl) via the vena jugularis after anesthesia with isoflurane inhalation and buprenorphine (0.1 mg/kg). After 1 hour of particle circulation, mice were anesthetized with ketamine (125 mg/kg of body weight) and xylazine (80 mg/kg of body weight),

the blood sample was collected, and they were euthanized through perfusion with DPBS. Subsequently, eyes, liver, heart, and kidneys were harvested, and the posterior part of one eye or 100 mg of each organ was homogenized in radioimmunoprecipitation assay buffer using an Ultra-Turrax tissue homogenizer (IKA). Then, samples were centrifuged (4 min, 4°C, 2000*g*), the supernatant was collected, and the nanoparticle concentration was determined using a FLUOstar Omega microplate reader and calculated using GraphPad Prism 6.0. To investigate the intraocular distribution, mice were treated with LNCs and RGD-LNCs loaded simultaneously with fluorescent dye (DiI) and SPIONs (dual LNC) as previously described (*37*). After either 1 hour, 24 hours, or 5 days of particle circulation, mice were anesthetized with ketamine (125 mg/kg of body weight) and xylazine (80 mg/kg of body weight) and euthanized through perfusion with 4% PFA, and eyes were enucleated. Afterward, one eye was cryoprotected by incubation in phosphate buffer (0.1 M, pH 7.4) supplemented with increasing sucrose concentrations (10, 20, and 30%) for 12 hours each, embedded in Tissue-Tek O.C.T. compound (Sakura Finetek), and subsequently frozen in liquid nitrogen. Last, they were cut into 12-µm sections using an HM 500 OM microtome (Microm International) and transferred onto Superfrost plus glass slides. To visualize choroid and retinal vessels, cryosections were washed with phosphate buffer (0.1 M, pH 7.4) before 1-hour blockage with 2% BSA supplemented with 0.2% cold water fish gelatin (CWFG) and 0.1% Triton X-100. Sections were then washed with phosphate buffer (3×, 5 min each) and incubated overnight with primary polyclonal goat anti-CD31 antibody (R&D Systems, Minneapolis, USA) (1:100 in 1:10 blockage buffer) at 4°C. Then, they were washed with phosphate buffer (3×, 5 min each) and incubated for 1 hour with biotinylated anti-goat secondary antibody (1:500 in 1:10 blockage buffer) (Vector Laboratories, Burlingame, USA). Before and after the incubation with streptavidin Alexa Fluor 488 (1:1000 in 1:10 blockage buffer) (Invitrogen, Thermo Fisher Scientific, Waltham, USA) for 1 hour, sections were washed again and rinsed with ultrapure water before mounting with Mowiol 4-88 (Carl Roth, Karlsruhe, Germany) supplemented with DAPI (0.15 µg/ml). Images were generated using an Axio Imager fluorescence microscope with a Plan-Neofluar 40×/1.30 oil M27 objective (Carl Zeiss AG) and the Zen software (Carl Zeiss Microscopy). For the quantitative evaluation of nanoparticle fluorescence in the RPE, the RPE area was gated, and the integrated fluorescence density of each gated area was quantified using ImageJ version 1.52. The other eye was used for the preparation of ultrathin sections for TEM. To that end, eyes were embedded in London resin white (Serva, Garden City Park, NY), and ultrathin sections (90 nm) were processed according to protocols published previously (*65*). TEM imaging was performed, as previously described, using a Libra 120 electron microscope (Carl Zeiss AG) (*65*).

Murine ROP model

The animal experiments regarding the assessment of nanoparticle efficacy were carried out according to institutional, national, and IACUC guidelines and were approved by the local authority (Regierung von Unterfranken, reference number: 55.2-2532-2-363). OIR was induced in mouse (129SV) pups according to a protocol previously established (*47*). Briefly, at P7, mouse pups and their nursing mothers were placed in a Plexiglas incubator with an adjustable oxygen sensor and feedback system and exposed to hyperoxia (75 ± 1% oxygen) for 5 days. On P12, the pups were returned to room-air conditions for another 5 days until P17. Mice were treated at P12 directly after returning to normoxia with either 20 µl of nanoparticle solution [RGD-LNCs or CsA RGD-LNCs (20 mg/ml)], CsA solution [Sandimmun (50 mg/ml), Novartis, Basel, Switzerland] diluted with isotonic saline solution to a final concentration of 0.68 mg/ml, or DPBS by injection via the vena jugularis after anesthesia with ketamine (125 mg/kg of body weight) and xylazine (80 mg/kg of body weight).

Assessment of ocular CsA content

To quantify the CsA content in the eye at P17 after the treatment with either CsA RGD-LNCs or free CsA on P12, mice were euthanized through cervical dislocation, eyes were enucleated, and the anterior parts including cornea and lens were discarded. Afterward, the posterior parts of the eye were weighed and homogenized in 0.5 ml of methanol using Ultra-Turrax tissue homogenizer (IKA) and ultrasonicated for 2 hours. Before the centrifugation (2000*g*, 30 min, 20°C), cyclosporin D (CsD) was added as internal standard (0.02 µg/ml). Last, the supernatant was analyzed, and the CsA content was determined using the same UHPLC-MS method as previously described (*38*). Data handling and processing were done using Microsoft Excel 2019 and GraphPad Prism 6.0.

Quantification of neovascularization

At P17, mice were weighed, and underdeveloped mice (<6 g) were excluded from further investigations. For the preparation of retina whole mounts, animals were anesthetized on P17 with ketamine (125 mg/kg of body weight) and xylazine (80 mg/kg of body weight). The heart was exposed through the diaphragm, and the left ventricle was injected with 1 ml of fluorescein isothiocyanate (FITC)–dextran (TdB, Uppsala, Sweden) solution in DPBS (50 mg/ml). Afterward, eyes were enucleated and placed in 4% PFA for 1 hour. Eye cups were dissected, and retinal flat mounts were created and examined using fluorescence microscopy (Axio Imager, Plan-Apochromat 20×/0.8 M27 objective). For quantitative analysis, the whole retinal area, avascular zone, and the area of vascular tortuosity, tufting, and leakiness were determined randomized and blinded using the Zen software (Carl Zeiss Microscopy).

Immunohistochemistry and immunofluorescence

The immunofluorescent detection of VEGF-R2 and GFAP was performed using cryosections. For the preparation of cryosections, mice were anesthetized at P17 with ketamine (125 mg/kg of body weight) and xylazine (80 mg/kg of body weight) and euthanized through perfusion fixation with 4% PFA, and afterward, eyes were enucleated and processed as described above. For VEGF-R2 staining, cryosections were washed with phosphate buffer (0.1 M, pH 7.4) before 1-hour blockage with 2% BSA supplemented with 0.2% CWFG. After the blockage, sections were washed again (3×, 5 min each) and incubated overnight with primary polyclonal rabbit anti-VEGFR2 antibody (Cell Signaling Technology, Danvers, USA) (1:200 in 1:10 blockage buffer) at 4°C. Then, they were washed (3×, 5 min each) and incubated for 1 hour with biotinylated anti-rabbit secondary antibody (1:500 in 1:10 blockage buffer) (Vector Laboratories, Burlingame, USA). After the incubation with streptavidin Alexa Fluor 488 (1:1000 in 1:10 blockage buffer) for 1 hour, sections were washed again and rinsed with ultrapure water before mounting with Mowiol 4-88 supplemented with DAPI (0.15 µg/ml). For GFAP staining, cryosections were washed with phosphate buffer (0.1 m) (pH 7.4) before the 1-hour blockage with 2% BSA supplemented

with 0.2% CWFG and 0.1% Triton X-100. After the blockage, sections were washed (3×, 5 min each) and incubated overnight with primary polyclonal chicken anti-GFAP antibody (LSBio, Seattle, USA) (1:1000 in 1:10 blockage buffer) at 4°C. Then, they were washed (3×, 5 min each) and incubated for 1 hour with Alexa Fluor 488 anti-chicken secondary antibody (1:1000 in 1:10 blockage buffer) (Abcam, Cambridge, UK). Last, the sections were washed again and rinsed with ultrapure water before mounting with Mowiol 4-88 supplemented with DAPI (0.15 µg/ml). Images were generated using an Axio Imager fluorescence microscope with a Plan-Neofluar 40×/1.30 oil M27 objective (Carl Zeiss AG) and the Zen software (Carl Zeiss Microscopy). For the quantitative evaluation of immunofluorescence in the whole posterior eye section, the ocular area was gated, and the integrated fluorescence density of each gated area was quantified using ImageJ version 1.52.

VEGF quantification

To assess the VEGF protein levels quantitatively, an enzyme-linked immunosorbent assay (ELISA) for mouse VEGF (R&D Systems, Minneapolis, USA) was used. For the generation of tissue samples, mice were euthanized through cervical dislocation, eyes were enucleated, and both the sensory retina and the RPE-choroid complex were collected. Samples were treated with 500 µl of TRIzol (Invitrogen, Waltham, USA), and for protein isolation, the manufacturer's instructions were followed. Afterward, 40 µl of sensory retina lysate or 100 µl of RPE-choroid lysate were diluted with sample diluent provided by the manufacturer up to 200 µl. VEGF measurements were then performed according to the provided protocol. Fluorescence was measured using a FLUOstar Omega microplate reader, and data were calculated using GraphPad Prism 6.0.

Reverse transcription polymerase chain reaction

RNA samples from both the sensory retina and the RPE-choroid complex were extracted using TRIzol (Invitrogen, Waltham, USA) following the manufacturer's instructions for RNA isolation. After determining the RNA concentration using a NanoDrop spectrophotometer (Thermo Fisher Scientific, Waltham, USA), equal amounts of total RNA were reverse-transcribed into first-strand cDNA using the iScript cDNA Synthesis Kit (Bio-Rad, Hercules, USA) according to the manufacturer's instructions. Quantitative real-time reverse transcription polymerase chain reaction (RT-PCR) analyses were performed using the iQ5 Real-Time PCR Detection System (Bio-Rad). RNA that was not reverse-transcribed served as negative control for real-time RT-PCR, and for relative quantification, GNB2L was used. Quantification and analysis were performed using Bio-Rad iQ5 software (Bio-Rad), and data were processed using Microsoft Excel 2019 and GraphPad Prism 6.0. The primer sequences (Invitrogen, Waltham, USA) used were as follows:

5′-TCTGCAAGTACACGGTCCAG-3′ (Gnb2l forward)
5′-GAGACGATGATAGGGTTGCTG-3′ (Gnb2l reverse)
5′-GAACAAAGCCAGAAAATCACTGTG-3′ (Vegf-a-164 forward)
5′-CGAGTCTGTGTTTTTGCAGGAAC-3′ (Vegf-a-164 reverse)
5′-CAGTGGTACTGGCAGCTAGAAG-3′ (VegfR2 forward)
5′-ACAAGCATACGGGCTTGTTT-3′ (VEGFR2 reverse)
5′-TCTTCCGCTTGCAAAACC-3′ (Tgfbeta2 forward)
5′-GTGGGAGATGTTAAGTCTTTGGA-3′ (Tgfbeta2 reverse)
5′-AGAAGCCGCATGAAGTCTG-3′ (TgfbetaR2 forward)
5′-GGCAAACCGTCTCCAGAGTA-3′ (TgfbetaR2 reverse)
5′-AGTTGACCGACCCCAAAAG-3′ (Il-1beta forward)
5′-AGCTGCATGCTCTGATCAGG-3′ (Il-1beta reverse)

Morphological examination

To detect morphological changes in the retina of mice caused by the therapeutic intervention, mice were anesthetized at P17 with ketamine (125 mg/kg of body weight) and xylazine (80 mg/kg of body weight) and euthanized through perfusion with 4% PFA. Then, eyes were enucleated, fixed for 24 hours in Ito's fixative, and embedded in Epon as previously described (*65*). Semi-thin sections of 1.0-µm thickness were cut along the mid-horizontal (nasal-temporal) plane and stained by Richardson's stain. Afterward, images were taken using light microscopy (Axio Imager, Plan-Neofluar 40×/1.30 oil M27 objective; Carl Zeiss). For a quantitative assessment, the distance between ora serrata and optic nerve head was divided into tenths, and the thickness of the outer nuclear layer and inner nuclear layer was measured between each tenth using Zen software (Carl Zeiss Microscopy) and ImageJ version 1.52. Data were handled using Microsoft Excel 2019 and GraphPad Prism 6.0.

Statistical analysis

Data are expressed as means ± SD. Statistical evaluation was performed using GraphPad Prism software 6.0. Student's *t* test for unpaired data, one-way analysis of variance (ANOVA), and two-way ANOVA with a Sidak's or Tukey's multiple comparison test were used to evaluate statistical significance. Levels of statistical significance and "*n*" numbers for each experiment are indicated in figure legends.

SUPPLEMENTARY MATERIALS

Supplementary material for this article is available at https://science.org/doi/10.1126/sciadv.abo6638

REFERENCES AND NOTES

1. J. P. Vogel, S. Chawanpaiboon, A.-B. Moller, K. Watananirun, M. Bonet, P. Lumbiganon, The global epidemiology of preterm birth. *Best Pract. Res. Clin. Obstet. Gynaecol.* **52**, 3–12 (2018).
2. S. J. Kim, A. D. Port, R. Swan, J. P. Campbell, R. V. P. Chan, M. F. Chiang, Retinopathy of prematurity: A review of risk factors and their clinical significance. *Surv. Ophthalmol.* **63**, 618–637 (2018).
3. A. Hellstrom, L. E. Smith, O. Dammann, Retinopathy of prematurity. *Lancet* **382**, 1445–1457 (2013).
4. O. Strauss, The retinal pigment epithelium in visual function. *Physiol. Rev.* **85**, 845–881 (2005).
5. P. S. Caceres, E. Rodriguez-Boulan, Retinal pigment epithelium polarity in health and blinding diseases. *Curr. Opin. Cell Biol.* **62**, 37–45 (2020).
6. M. E. Hartnett, Pathophysiology and mechanisms of severe retinopathy of prematurity. *Ophthalmology* **122**, 200–210 (2015).
7. J. C. Rivera, M. Holm, D. Austeng, T. S. Morken, T. E. Zhou, A. Beaudry-Richard, E. M. Sierra, O. Dammann, S. Chemtob, Retinopathy of prematurity: Inflammation, choroidal degeneration, and novel promising therapeutic strategies. *J. Neuroinflammation* **14**, 165 (2017).
8. GBD 2015 Healthcare Access and Quality Collaborators, Healthcare Access and Quality Index based on mortality from causes amenable to personal health care in 195 countries and territories, 1990–2015: A novel analysis from the Global Burden of Disease Study 2015. *Lancet* **390**, 231–266 (2017).
9. G. L. Darmstadt, M. V. Kinney, M. Chopra, S. Cousens, L. Kak, V. K. Paul, J. Martines, Z. A. Bhutta, J. E. Lawn, Who has been caring for the baby? *Lancet* **384**, 174–188 (2014).
10. G. E. Quinn, Retinopathy of prematurity blindness worldwide: Phenotypes in the third epidemic. *Eye Brain* **8**, 31–36 (2016).
11. L. E. H. Smith, Through the eyes of a child: Understanding retinopathy through ROP the Friedenwald lecture. *Invest. Ophthalmol. Vis. Sci.* **49**, 5177–5182 (2008).
12. H. Blencowe, S. Cousens, D. Chou, M. Oestergaard, L. Say, A.-B. Moller, M. Kinney, J. Lawn, Born too soon: The global epidemiology of 15 million preterm births. *Reprod. Health* **10**, S2 (2013).
13. J. D. Steinmetz, R. R. A. Bourne, P. S. Briant, S. R. Flaxman, H. R. B. Taylor, J. B. Jonas, A. A. Abdoli, W. A. Abrha, A. Abualhasan, E. G. Abu-Gharbieh, T. G. Adal, A. Afshin,

H. Ahmadieh, W. Alemayehu, S. A. S. Alemzadeh, A. S. Alfaar, V. Alipour, S. Androudi, J. Arabloo, A. B. Arditi, B. B. Aregawi, A. Arrigo, C. Ashbaugh, E. D. Ashrafi, D. D. Atnafu, E. A. Bagli, A. A. W. Baig, T. W. Bärnighausen, M. Battaglia Parodi, M. S. Beheshti, A. S. Bhagavathula, N. Bhardwaj, P. Bhardwaj, K. Bhattacharyya, A. Bijani, M. Bikbov, M. Bottone, T. M. Braithwaite, A. M. Bron, S. A. Burugina Nagaraja, Z. A. Butt, F. L. L. Caetano dos Santos, V. L. J. Carneiro, R. J. Casson, C.-Y. J. Cheng, J.-Y. J. Choi, D. T. Chu, M. V. M. Cicinelli, J. M. G. Coelho, N. G. A. Congdon, R. A. A. Couto, E. A. M. Cromwell, S. M. Dahlawi, X. Dai, R. Dana, L. Dandona, R. A. Dandona, M. A. del Monte, M. Derbew Molla, N. A. Dervenis, A. A. P. Desta, J. P. Deva, D. Diaz, S. E. Djalalinia, J. R. Ehrlich, R. R. Elayedath, H. R. B. Elhabashy, L. B. Ellwein, M. H. Emamian, S. Eskandarieh, F. G. Farzadfar, A. G. Fernandes, F. S. Fischer, D. S. M. Friedman, J. M. Furtado, S. Gaidhane, G. Gazzard, B. Gebremichael, R. George, A. Ghashghaee, S. A. Gilani, M. Golechha, S. R. Hamidi, B. R. R. Hammond, M. E. R. K. Hartnett, R. K. Hartono, A. I. Hashi, S. I. Hay, K. Hayat, G. Heidari, H. C. Ho, R. Holla, M. J. Househ, J. J. E. Huang, S. E. M. Ibitoye, I. M. D. Ilic, M. D. D. Ilic, A. D. N. Ingram, S. S. N. Irvani, S. M. S. Islam, R. Itumalla, S. P. Jayaram, R. P. Jha, R. Kahloun, R. Kalhor, H. Kandel, A. S. Kasa, T. A. Kavetskyy, G. A. H. Kayode, J. H. Kempen, M. Khairallah, R. A. Khalilov, E. A. C. Khan, R. C. Khanna, M. N. A. Khatib, T. A. E. Khoja, J. E. Kim, Y. J. Kim, G. R. Kim, S. Kisa, A. Kisa, S. Kosen, A. Koyanagi, B. Kucuk Bicer, V. P. Kulkarni, O. P. Kurmi, I. C. Landires, V. C. L. Lansingh, J. L. E. Leasher, K. E. LeGrand, N. Leveziel, H. Limburg, X. Liu, S. Madhava Kunjathur, S. Maleki, N. Manafi, K. Mansouri, C. G. McAlinden, G. G. M. Meles, A. M. Mersha, I. M. R. Michalek, T. R. Miller, S. Misra, Y. Mohammad, S. F. A. Mohammadi, J. A. H. Mohammed, A. H. Mokdad, M. A. A. Moni, A. A. R. Montasir, A. R. F. Morse, G. F. C. Mulaw, M. Naderi, H. S. Naderifar, K. S. Naidoo, M. D. Naimzada, V. Nangia, S. M. Narasimha Swamy, D. M. Naveed, H. L. Negash, H. L. Nguyen, V. A. Nunez-Samudio, F. A. Ogbo, K. T. Ogundimu, A. T. E. Olagunju, O. E. Onwujekwe, N. O. Otstavnov, M. O. Owolabi, K. Pakshir, S. Panda-Jonas, U. Parekh, E. C. Park, M. Pasovic, S. Pawar, K. Pesudovs, T. Q. Peto, H. Q. Pham, M. Pinheiro, V. Podder, V. Rahimi-Movaghar, M. H. U. Y. Rahman, P. Y. Ramulu, P. Rathi, S. L. Rawaf, D. L. Rawaf, L. Rawal, N. M. Reinig, A. M. Renzaho, A. L. Rezapour, A. L. Robin, L. Rossetti, S. Sabour, S. Safi, A. Sahebkar, M. A. M. Sahraian, A. M. Samy, B. Sathian, G. K. Saya, M. A. Saylan, A. A. A. Shaheen, M. A. T. Shaikh, T. T. Shen, K. S. Shibuya, W. S. Shiferaw, M. Shigematsu, J. I. Shin, J. C. Silva, A. A. Silvester, J. A. Singh, D. S. Singhal, R. S. Sitorus, E. Y. Skiadaresi, V. Y. A. Skryabin, A. A. Skryabina, A. B. Soheili, M. B. A. R. C. Sorrie, R. A. R. C. T. Sousa, C. T. Sreeramareddy, D. G. Stambolian, E. G. Tadesse, N. I. Tahhan, M. I. Tareque, F. X. Topouzis, B. X. Tran, G. K. Tsegaye, M. K. Tsilimbaris, R. Varma, G. Virgili, A. T. Vongpradith, G. T. Vu, Y. X. Wang, N. H. Wang, A. H. K. Weldemariam, S. K. G. West, T. G. Y. Wondmeneh, T. Y. Wong, M. Yaseri, N. Yonemoto, C. S. Yu, M. S. Zastrozhin, Z.-J. R. Zhang, S. R. Zimsen, S. Resnikoff, T. Vos, Causes of blindness and vision impairment in 2020 and trends over 30 years, and prevalence of avoidable blindness in relation to VISION 2020: The right to sight: An analysis for the Global Burden of Disease Study. *Lancet Glob. Health* **9**, e144–e160 (2021).

14. H. A. Mintz-Hittner, K. A. Kennedy, A. Z. Chuang, Efficacy of intravitreal bevacizumab for stage 3+ retinopathy of prematurity. *N. Engl. J. Med.* **364**, 603–615 (2011).
15. A. S. Maharaj, M. Saint-Geniez, T. E. Walshe, E. Sekiyama, T. Kurihara, B. Tucker, M. Young, P. A. D'Amore, VEGF is required for neuroretina survival and function. *Invest. Ophthalmol. Vis. Sci.* **49**, 5836 (2008).
16. J. I. Greenberg, D. J. Shields, S. G. Barillas, L. M. Acevedo, E. Murphy, J. Huang, L. Scheppke, C. Stockmann, R. S. Johnson, N. Angle, D. A. Cheresh, A role for VEGF as a negative regulator of pericyte function and vessel maturation. *Nature* **456**, 809–813 (2008).
17. A.-L. Wu, W.-C. Wu, Anti-VEGF for ROP and pediatric retinal diseases. *Asia Pac. J. Ophthalmol.* **7**, 145–151 (2018).
18. K. D. Tran, L. A. Cernichiaro-Espinosa, A. M. Berrocal, Management of retinopathy of prematurity—Use of anti-VEGF therapy. *Asia Pac. J. Ophthalmol.* **7**, 56–62 (2018).
19. A. Urtti, Challenges and obstacles of ocular pharmacokinetics and drug delivery. *Adv. Drug Deliv. Rev.* **58**, 1131–1135 (2006).
20. M. Bohley, A. E. Dillinger, E. R. Tamm, A. Goepferich, Targeted drug delivery to the retinal pigment epithelium: Untapped therapeutic potential for retinal diseases. *Drug Discov. Today*, S1359-6446(22)00215-X (2022).
21. H. Xu, M. Chen, Targeting the complement system for the management of retinal inflammatory and degenerative diseases. *Eur. J. Pharmacol.* **787**, 94–104 (2016).
22. E. M. del Amo, A.-K. Rimpelä, E. Heikkinen, O. K. Kari, E. Ramsay, T. Lajunen, M. Schmitt, L. Pelkonen, M. Bhattacharya, D. Richardson, A. Subrizi, T. Turunen, M. Reinisalo, J. Itkonen, E. Toropainen, M. Casteleijn, H. Kidron, M. Antopolsky, K.-S. Vellonen, M. Ruponen, A. Urtti, Pharmacokinetic aspects of retinal drug delivery. *Prog. Retin. Eye Res.* **57**, 134–185 (2017).
23. Q. Li, J. Weng, S. N. Wong, W. Y. Thomas Lee, S. F. Chow, Nanoparticulate drug delivery to the retina. *Mol. Pharm.* **18**, 506–521 (2020).
24. E. Blanco, H. Shen, M. Ferrari, Principles of nanoparticle design for overcoming biological barriers to drug delivery. *Nat. Biotechnol.* **33**, 941–951 (2015).
25. K. C. Hayes, S. Lindsey, Z. F. Stephan, D. Brecker, Retinal pigment epithelium possesses both LDL and scavenger receptor activity. *Invest. Ophthalmol. Vis. Sci.* **30**, 225–232 (1989).
26. I. A. Pikuleva, C. A. Curcio, Cholesterol in the retina: The best is yet to come. *Prog. Retin. Eye Res.* **41**, 64–89 (2014).
27. N. Gordiyenko, M. Campos, J. W. Lee, R. N. Fariss, J. Sztein, I. R. Rodriguez, RPE cells internalize low-density lipoprotein (LDL) and oxidized LDL (oxLDL) in large quantities in vitro and in vivo. *Invest. Ophthalmol. Vis. Sci.* **45**, 2822–2829 (2004).
28. N. Kuno, S. Fujii, Recent advances in ocular drug delivery systems. *Polymers* **3**, 193–221 (2011).
29. D. Calvo, D. Gómez-Coronado, Y. Suárez, M. A. Lasunción, M. A. Vega, Human CD36 is a high affinity receptor for the native lipoproteins HDL, LDL, and VLDL. *J. Lipid Res.* **39**, 777–788 (1998).
30. M. Friedlander, C. L. Thehsfeld, M. Sugita, M. Fruttiger, M. A. Thomas, S. Chang, D. A. Cheresh, Involvement of integrins alpha v beta 3 and alpha v beta 5 in ocular neovascular diseases. *Proc. Natl. Acad. Sci. U.S.A.* **93**, 9764–9769 (1996).
31. M. Kato, M. Mrksich, Using model substrates to study the dependence of focal adhesion formation on the affinity of integrin-ligand complexes. *Biochemistry* **43**, 2699–2707 (2004).
32. C. L. Modery-Pawlowski, A. Sen Gupta, Heteromultivalent ligand-decoration for actively targeted nanomedicine. *Biomaterials* **35**, 2568–2579 (2014).
33. P. Rafiee, J. Heidemann, H. Ogawa, N. A. Johnson, P. J. Fisher, M. S. Li, M. F. Otterson, C. P. Johnson, D. G. Binion, Cyclosporin A differentially inhibits multiple steps in VEGF induced angiogenesis in human microvascular endothelial cells through altered intracellular signaling. *Cell Commun. Signal* **2**, 3 (2004).
34. D. J. Freeman, Pharmacology and pharmacokinetics of cyclosporine. *Clin. Biochem.* **24**, 9–14 (1991).
35. J. F. Borel, C. Feurer, H. U. Gubler, H. Stähelin, Biological effects of cyclosporin A: A new antilymphocytic agent. 1976. *Agents Actions* **43**, 179–186 (1994).
36. S. Schnichels, M. Schultheiss, P. Klemm, M. Blak, T. Herrmann, M. Melchinger, K.-U. Bartz-Schmidt, M. Löscher, G. Zeck, M. S. Spitzer, J. Hurst, Cyclosporine A protects retinal explants against hypoxia. *Int. J. Mol. Sci.* **22**, 10196 (2021).
37. V. C. Chow, R. P. Pai, J. R. Chapman, P. J. O'connell, R. D. Allen, P. Mitchell, B. J. Nankivell, Diabetic retinopathy after combined kidney-pancreas transplantation. *Clin. Transpl.* **13**, 356–362 (1999).
38. M. Bohley, A. Haunberger, A. Goepferich, Intracellular availability of poorly soluble drugs from lipid nanocapsules. *Eur. J. Pharm. Biopharm.* **139**, 23–32 (2019).
39. T. R. Thrimawithana, S. Young, C. R. Bunt, C. Green, R. G. Alany, Drug delivery to the posterior segment of the eye. *Drug Discov. Today* **16**, 270–277 (2011).
40. S. Wilhelm, A. J. Tavares, Q. Dai, S. Ohta, J. Audet, H. F. Dvorak, W. C. W. Chan, Analysis of nanoparticle delivery to tumours. *Nat. Rev. Mater.* **1**, 16014 (2016).
41. K. Pollinger, R. Hennig, A. Ohlmann, R. Fuchshofer, R. Wenzel, M. Breunig, J. Tessmar, E. R. Tamm, A. Goepferich, Ligand-functionalized nanoparticles target endothelial cells in retinal capillaries after systemic application. *Proc. Natl. Acad. Sci. U.S.A.* **110**, 6115–6120 (2013).
42. M. S. Bohley, E. Birch, F. J. Baumann, A. E. Dillinger, E. R. Tamm, A. M. Goepferich, Design of dye and superparamagnetic iron oxide nanoparticle loaded lipid nanocapsules with dual detectability in vitro and in vivo. *Int. J. Pharm.* **585**, 119433 (2020).
43. A. Scott, M. Fruttiger, Oxygen-induced retinopathy: A model for vascular pathology in the retina. *Eye* **24**, 416–421 (2010).
44. B. K. Clifford, A. P. D'Amore, K. M. Connor, Revisiting the mouse model of oxygen-induced retinopathy. *Eye Brain* **8**, 67–79 (2016).
45. S. Rathi, S. Jalali, S. Patnaik, S. Shahulhameed, G. R. Musada, D. Balakrishnan, P. K. Rani, R. Kekunnaya, P. P. Chhablani, S. Swain, L. Giri, S. Chakrabarti, I. Kaur, Abnormal complement activation and inflammation in the pathogenesis of retinopathy of prematurity. *Front. Immunol.* **8**, 1868 (2017).
46. K. H. J. Ehinger, M. J. Hansson, F. Sjövall, E. Elmér, Bioequivalence and tolerability assessment of a novel intravenous ciclosporin lipid emulsion compared to branded ciclosporin in Cremophor ® EL. *Clin. Drug Investig.* **33**, 25–34 (2013).
47. K. M. Connor, N. M. Krah, R. J. Dennison, C. M. Aderman, J. Chen, K. I. Guerin, P. Sapieha, A. Stahl, K. L. Willett, L. E. H. Smith, Quantification of oxygen-induced retinopathy in the mouse: A model of vessel loss, vessel regrowth and pathological angiogenesis. *Nat. Protoc.* **4**, 1565–1573 (2009).
48. Z.-M. Bian, S. G. Elner, V. M. Elner, Regulation of VEGF mRNA expression and protein secretion by TGF-β2 in human retinal pigment epithelial cells. *Exp. Eye Res.* **84**, 812–822 (2007).
49. B. A. Nacev, J. O. Liu, Synergistic inhibition of endothelial cell proliferation, tube formation, and sprouting by cyclosporin A and itraconazole. *PLOS ONE* **6**, e24793 (2011).
50. R. M. Kurtz, V. M. Elner, Z. M. Bian, R. M. Strieter, S. L. Kunkel, S. G. Elner, Dexamethasone and cyclosporin A modulation of human retinal pigment epithelial cell monocyte chemotactic protein-1 and interleukin-8. *Invest. Ophthalmol. Vis. Sci.* **38**, 436–445 (1997).
51. A. Reichenbach, A. Bringmann, New functions of Müller cells. *Glia* **61**, 651–678 (2013).
52. N. Bertrand, J.-C. Leroux, The journey of a drug-carrier in the body: An anatomo-physiological perspective. *J. Control. Release* **161**, 152–163 (2012).

53. S. R. Singh, H. E. Grossniklaus, S. J. Kang, H. F. Edelhauser, B. K. Ambati, U. B. Kompella, Intravenous transferrin, RGD peptide and dual-targeted nanoparticles enhance anti-VEGF intraceptor gene delivery to laser-induced CNV. *Gene Ther.* **16**, 645–659 (2009).
54. C. Zhu, Y. Zhang, W. M. Pardridge, Widespread expression of an exogenous gene in the eye after intravenous administration. *Invest. Ophthalmol. Vis. Sci.* **43**, 3075–3080 (2002).
55. N. Erol, H. Gursoy, S. Kimyon, S. Topbas, E. Colak, Vision, retinal thickness, and foveal avascular zone size after intravitreal bevacizumab for diabetic macular edema. *Adv. Ther.* **29**, 359–369 (2012).
56. M.-Y. Hsu, Y.-C. Hung, D.-K. Hwang, S.-C. Lin, K.-H. Lin, C.-Y. Wang, H.-Y. Choi, Y.-P. Wang, C.-M. Cheng, Detection of aqueous VEGF concentrations before and after intravitreal injection of anti-VEGF antibody using low-volume sampling paper-based ELISA. *Sci. Rep.* **6**, 34631 (2016).
57. B. G. Sood, A. Madan, S. Saha, D. Schendel, P. Thorsen, K. Skogstrand, D. Hougaard, S. Shankaran, W. Carlo; NICHD neonatal research network, Perinatal systemic inflammatory response syndrome and retinopathy of prematurity. *Pediatr. Res.* **67**, 394–400 (2010).
58. J. E. Sears, G. Hoppe, Q. Ebrahem, B. Anand-Apte, Prolyl hydroxylase inhibition during hyperoxia prevents oxygen-induced retinopathy. *Proc. Natl. Acad. Sci. U.S.A.* **105**, 19898–19903 (2008).
59. G. Hoppe, S. Yoon, B. Gopalan, A. R. Savage, R. Brown, K. Case, A. Vasanji, E. R. Chan, R. B. Silver, J. E. Sears, Comparative systems pharmacology of HIF stabilization in the prevention of retinopathy of prematurity. *Proc. Natl. Acad. Sci. U.S.A.* **113**, E2516–E2525 (2016).
60. C. Singh, G. Hoppe, V. Tran, L. McCollum, Y. Bolok, W. Song, A. Sharma, H. Brunengraber, J. E. Sears, Serine and 1-carbon metabolism are required for HIF-mediated protection against retinopathy of prematurity. *JCI Insight* **4**, e129398 (2019).
61. A. Qadri, C. L. Cai, K. Deslouches, F. Siddiqui, J. V. Aranda, K. D. Beharry, Ocular versus oral propranolol for prevention and/or treatment of oxygen-induced retinopathy in a rat model. *J. Ocul. Pharmacol. Ther.* **37**, 112–130 (2021).
62. D. Ley, B. Hallberg, I. Hansen-Pupp, C. Dani, L. A. Ramenghi, N. Marlow, K. Beardsall, F. Bhatti, D. Dunger, J. D. Higginson, A. Mahaveer, O. J. Mezu-Ndubuisi, P. Reynolds, C. Giannantonio, M. van Weissenbruch, N. Barton, A. Tocoian, M. Hamdani, E. Jochim, A. Mangili, J.-K. Chung, M. A. Turner, L. E. H. Smith, A. Hellström; study team, rhIGF-1/rhIGFBP-3 in preterm infants: A phase 2 randomized controlled trial. *J. Pediatr.* **206**, 56–65.e8 (2019).
63. B. Heurtault, P. Saulnier, B. Pech, J.-E. Proust, J.-P. Benoit, A novel phase inversion-based process for the preparation of lipid nanocarriers. *Pharm. Res.* **19**, 875–880 (2002).
64. T. Perrier, P. Saulnier, F. Fouchet, N. Lautram, J.-P. Benoît, Post-insertion into Lipid NanoCapsules (LNCs): From experimental aspects to mechanisms. *Int. J. Pharm.* **396**, 204–209 (2010).
65. B. Braunger, V. S. Leimbeck, A. Schlecht, C. Volz, H. Jägle, E. Tamm, Deletion of ocular transforming growth factor β signaling mimics essential characteristics of diabetic retinopathy. *Am. J. Clin. Pathol.* **185**, 1749–1768 (2015).

Acknowledgments: We thank R. Liebl, S. Babl, E. Stauber, A. Pach, and J. Kiermaier for excellent technical assistance. Parts of the data are subject to a patent application (PCT/EP2021/056231). **Funding:** This work was funded by the German Research Foundation (DFG) (GO 565/18-1) (to A.G. and E.R.T.). **Author contributions:** Conceptualization: M.B., A.G., E.R.T., and B.M.B. Methodology: M.B., A.E.D., A.O., B.M.B., E.R.T., and A.G. Investigation: M.B., A.E.D., and F.S. Visualization: M.B. Funding acquisition: A.G. and E.R.T. Project administration: M.B., A.E.D., A.G., and E.R.T. Supervision: A.G. and E.R.T. Writing—original draft: M.B. and A.G. Writing—review and editing: M.B., A.E.D., F.S., A.O., B.M.B., E.R.T., and A.G. **Competing interests:** M.B. and A.G. are inventors on a patent application related to this work filed by University Regensburg, Germany (PCT/EP2021/056231; filed 11 March 2021, published 16 September 2021). The authors declare that they have no other competing interests. **Data and materials availability:** All data needed to evaluate the conclusions in the paper are present in the paper and/or the Supplementary Materials.

Submitted 17 February 2022
Accepted 4 August 2022
Published 23 September 2022
10.1126/sciadv.abo6638